

Three Dimensional Shear Velocity Structure of Crust and Upper Mantle
in China From Ambient Noise Surface Wave Tomography

Xinlei Sun^{1,\$}, Xiaodong Song¹, Sihua Zheng^{1,2}, Yingjie Yang³, Mike Ritzwoller³

¹ Department of Geology, University of Illinois at Urbana-Champaign, IL, 61801

² Institute of Earthquake Science, China Earthquake Administration, No. 63, Fuxing Avenue, Beijing, 100036, China

³ CIEI, Department of Physics, University of Colorado at Boulder, Boulder, CO, 80309

^{\$} Now at Department of Earth and Planetary Sciences, Washington University in St. Louis, St. Louis, MO, 63130

Abstract We determine the 3D shear velocity structure of the crust and upper mantle in China using Green's functions obtained from seismic ambient noise cross-correlation. The data we used are from the China National Seismic Network, global and regional network and PASSCAL stations in the region. We first acquire cross-correlation seismogram between all possible station pairs. We then extract the Rayleigh wave group and phase dispersion curves using frequency-time analysis method from 8 to 60s. After that, Rayleigh wave group and phase velocity dispersion maps at 1 by 1 degree grids are obtained at different period. And finally, 3D shear velocity structure of the crust and upper mantle in China is inverted from the dispersion curves at each grid. The inversion results show many large-scale structures that correlate with surface geology. Near the surface, velocities in major basins are anomalously

slow, consistent with the thick sediments. East-west contrasts are striking in Moho depth and lithosphere thickness. Also, There exists a fast mid-lower crust and mantle lithosphere in major basins surrounding the Tibet Plateau (TP) and Tianshan (Junggar, Tarim, Ordos, and Sichuan). These strong blocks thus seem to play an important role in confining the deformation of the TP to be a triangular shape. In northwest TP in Qiangtang, slow anomalies extend from crust to great depth in mantle lithosphere. Meanwhile, widespread, prominent low-velocity zone is observed in mid-crust in most of the central, eastern and southeastern Tibet Plateau, consistent with a weak (and perhaps mobile) mid-crust.

1 Introduction

Located in the southeast part of Eurasia, China and its surrounding areas are geologically diverse and tectonically active. It is basically several old ancient platforms (e.g., Sino-Korea , Yangtz craton), deep sedimentary basins (e.g., Ordos and Tarim basin), and high plateau (Tibet) separated by active structures such as faults and series of mountains and fold belts (Fig.1). Two major events are mostly responsible for the complex features in this region: 1) Collision between India and Eurasia Plate about 50 Ma ago (Molnar and Tapponnier, 1975; Yin and Harrison, 2000, and 2) Subduction of Pacific Plate underneath Eurasia since about 250 Ma. As a result, the collision and post collision of India-Eurasia has led to the shortening and elevation of Tibet plateau; and the subduction of Pacific and Philippine plate led to the formation of island arcs, continental rift zones. Between these convergent boundaries, extensions are common features such as the extension in Sino-China block (Nabelek et al., 1987; Ying et al., 2006), and in Tibet Plateau (Armijo et al., 1986; Blisniuk et al., 2001; Turner et al., 1996; Williams et al., 2001; Zhang et al., 2004).

To understand the mechanism, history and the relationships between these unique tectonic features, the detailed structure of the crust and upper mantle in China and its surrounding areas is highly needed.

Seismic tomography is very useful and powerful tool to investigate the structure of China. Quite a few body wave and surface wave tomography studies have been conducted in China and surrounding areas (Friederich, 2003; Huang et al., 2003; Li et al., 2006; Liang et al., 2004; Ritzwoller et al., 1998; Shapiro et al., 2004; Sun and Toksoz, 2006; Wu et al., 1997). But these earthquake-generated data have their own limitations: commonly, because of the uneven distribution of earthquakes and available stations, the coverage of these data is generally sparse and non-uniform. Body waves especially have sparse coverage in the crust and upper mantle of the Earth from far field earthquakes, while surface waves at short periods are difficult to get due to attenuation and scattering effect, not to mention they have long wavelength and lower lateral resolution. Although there are general agreements for the large-scale structure, discrepancy remains for the smaller structure, which may be key factor to unravel the paths of tectonic revolutions. In recent years, a lot of efforts have been carried on to study the detailed structure using local and temporary seismic arrays. Unfortunately, they are mainly focus on some local area, especially in Tibet region (Hauck et al., 1998; Liang and Song, 2006; Nelson et al., 1996; Sandvol et al., 1997; Tilmann and Ni, 2003; Tseng et al., 2009; Zhao et al., 2001). We still need a detailed structure at continental scale in order to fully understand the dynamics and tectonic evolutions in the whole China region.

Recent studies have shown that surface wave can be easily retrieved from seismic coda waves (Campillo and Paul, 2003; Paul et al., 2005) or

seismic ambient noise (Sabra et al., 2005a; Sabra et al., 2005c; Shapiro and Campillo, 2004). This method overcomes shortcomings of earthquake-generated signals. First, The path density only depends on the distribution of stations. More dense and uniform coverage can be obtained between station pairs. This is especially helpful in aseismic regions; Secondly, uncertainties of earthquake locations, origin times and phases can be avoided, since no earthquake information is needed; Third, good short period surface waves can be extracted, while this is not true for conventional signals due to high attenuation and long earthquake-station paths. Thus, the surface waves from ambient noise are generally better in constraining the shallower structure, especially in the crust. This new type of data has been quickly applied to different regions such as in continental scale and regional scale (Bensen et al., 2007; Bensen et al., 2008; Li et al., 2009; Lin et al., 2008; Moschetti et al., 2007; Sabra et al., 2005b; Shapiro et al., 2005; Yang et al., 2007; Yao et al., 2008; Zheng et al., 2008), and has demonstrated promising results in terms of crust and upper mantle structure in detail.

In this study, we use the data from new Chinese National Seismic Network (CNSN) across China, permanent and regional stations from surrounding areas and PASSCAL experiments in this region (Fig. 1). The CNSN is deployed since year 2000, and is the backbone network in the whole China region. The addition of CNSN stations and PASSCAL stations has greatly improved the data coverage. Meanwhile, it makes the ray path coverage more uniform, especially in east part of China. We use vertical component of seismogram only and focus on Rayleigh wave group and phase dispersion curves. Part of the data has been used in Zheng et al. (Zheng et al., 2008). We obtain the surface wave dispersion curves between station pairs from the stacked ambient noise cross-

correlation, and then use tomography method to get the dispersion maps. Finally we invert the 1D shear velocity structure underneath about 2400 grid locations, and then combine them to construct a 3D shear velocity map in the crust and upper mantle of China. Our results generally show correlations between structures and surface geology. Some remarkable features such as the mid/lower crust low velocity zone beneath most of Tibet may also shed some light in understanding the tectonic dynamics there.

2 Data and Method

The data we used are 18 months vertical-component continuous seismograms from 48 China National Seismic Network (CNSN) stations, 32 global and regional networks stations in the surrounding area (the IRIS global seismic network, TW, KZ and KN networks), and 96 PASSCAL stations deployed in Tibet and Sichuan basin during the same period (Namche Barwa and 2003MIT-China) (Fig.1). All these data are broadband. Part of our data, such as data from the CNSN stations, is the same as in Zheng et al. (Zheng et al., 2008). When the stations of regional and PASSCAL network are added, the general ray coverage is very well improved (a typical ray density can be seen in Fig. 2).

The general process for our inversion is, first, we obtain empirical Green's function (EGF) for Rayleigh waves between all the station pairs. The process we used here is described in detail in Bensen et al. (Bensen et al., 2007). Basically, what we do is, we remove the instrument response and do clock synchronization, time-domain filtering (5-150 s period), and spectral whitening. We then do cross correlation on each day's seismogram between all possible stations, and stack all the

correlation to finally get the EGF. We carefully choose the good data by examine the signal to noise ratio (we use $SNR > 10$) for the EGFs and with distance at least 3 times of wavelength for that period. After this selection, only about 30-50% of the data remain. Secondly, we use a frequency-time analysis (FTAN) (Levshin and Ritzwoller, 2001) to get the Rayleigh wave group and phase velocity dispersion curves between station pairs from the selected EGFs. Third, The group and phase velocity tomography maps in this region is then constructed (Barmin et al., 2001) at 1 by 1 degree (Fig. 4). After that, a pure path dispersion curves at each grid node are obtained from the tomography maps at different periods. Finally, 1-D shear velocity structure of the crust and upper mantle under each grid node (Hermann, 2004) are inverted to construct a 3-D shear velocity map.

The dispersion curves we use are from 8 s to 60 s. The total ray path for each period is generally several thousand, with the best one of more than 7500 at 20s and the worst one of around 3300 at 60 s (Fig. 2). Fig. 2 also shows a ray density map at 20 s for the tomography. We can see that the best coverage is centered in east Tibet and Sichuan basin. This is understandable, because the two PASSCAL experiment there can generate the most abundant station pairs in that region. In the surrounding area, the ray coverage deteriorates gradually, but most of the density in each cell in the region is at least 100, which guarantee a reliable tomography result.

We assume that the group and phase velocities are isotropic at different period, and following Barmin et al (Barmin et al., 2001), we minimize the following equation to get the best model that fits the data.

$$(G(m) - d)^T C^{-1} (G(m) - d) + \alpha^2 \|F(m)\|^2 + \beta^2 \|H(m)\|^2$$

This equation is a combination of data misfit (first term), spatial smoothing (second term) and perturbations relative to reference model based on path density (third term).

The spatial smoothing is defined as

$$F(m) = m(r) - \int s(r, r') m(r') dr'$$

$$s(r, r') = K \exp\left(-\frac{|r - r'|^2}{2\sigma^2}\right)$$

In above equations, α, σ, β are damping for smoothing, the smoothing width, and damping for perturbation, respectively. The choice of these numbers is kind of arbitrary, and usually needs tests based on different data.

To ensure that the result is not affected by strange outliers, two step tomography are used. In the first tomography, we use a set of relatively large regularization factors to make a smoother map. Then based on the smooth mode, we calculated the predicted travel times for all data. The residuals fall out of 2 standard deviations of all residuals are discarded. Then using the new selected data, the second tomography is performed. This time, we tried different smoothing and damping factors (usually smaller than those of the first step). The resulted images are then compared. We use the good correlations of the image with the major surface features at short period as reference to choose the preferred ones. At the same time, if the tomography images also show reasonably detailed structure in the region, we choose it as our final model. Too

smoother and too dramatically changed images are discarded. This ensures reliability of our next inversion for shear velocity structure.

From the Rayleigh wave group and phase velocity maps obtained by above tomography, we extract the dispersion curves of group and phase velocity under each grid.

Using a program developed by Hermann and Ammon (Hermann,2004), we then invert the 1D shear velocity structure under each grid node. The velocities in between the nodes are interpolated using linear method. In this way a 3D shear velocity structure are constructed. The starting model for shear wave inversion is adopted from AK135 model with 25 layers overlying on a half space. The thickness of the layer is 5 km for the first 50 km, 10 km for the next 100 km, and then 25 km for the next 5 layers. In each layer, constant velocity and density are assumed. Since Rayleigh wave dispersion curves are mostly sensitive to shear velocity, only shear velocities are inverted in the inversion program, and the P wave and density of the layer are calculated from shear velocity using imperial functions.

The main consideration of the layer thickness division is based on the characteristics of our dispersion velocities and the resolution power of the surface waves. At shorter period (<30 s), the ray coverage is pretty good at nearly all our inversion regions, thus we are more confident about the Rayleigh wave velocity we get; Meanwhile, the sensitivity thickness of the surface wave is thinner, since the wavelength is shorter (See Fig. 7). When the period gets longer, the sparser ray coverage gives a more smoother velocity distribution in our inversion, and the thickness sensitivity of the wavelength are becoming broader, thus we have a

thicker layer at depth. We tested the surface wave inversion program with different type of models with different thickness. It turns out that with our data distribution, a 5 km layer can all be well resolved at shallow depth. If the layer is thinner, whether we can recover it or not depends on the type of velocity model.

To test the resolution of our inversion, we performed a checker board test. Like our starting model in the inversion, the test model we have is also adopted from ak135 model. It has the same layer distribution as in our starting model, but with $\pm 5\%$ velocity variations at alternative grid nodes. From the “real” models under each grid node, first we synthesize the pure path dispersion curves from 8 to 60~ s for Rayleigh wave group and phase velocities. Velocity maps at different period are then constructed. At each period, we then use the exact ray path (station pairs) as in our real data to generate the travel times and average velocity for all the paths. In this process, 1~s random noise are added to the travel times of all the ray paths. Using the average group and phase velocity for paths at different periods as the synthetic data, we performed the same inversion as described previously, that is, get tomography maps for group and phase velocity at each period, then generate pure path dispersion curves under each grid, and finally invert for shear velocity structure under each grid to generate a 3-D map of shear velocity. The inverted results can serve as a reference for resolution power.

Fig. 3 is the resulted resolution at different depth for a 4 by 4 degree pattern. Although the amplitude of the velocity variation is underestimated (generally about 3%), it is clearly seen that nearly at all the depth (from 2.5 km to 85 km), the velocity pattern can be retrieved pretty good, especially for the shallow and mid/lower crust depth. Our

resolution is the best in east and south Tibet region and Sichuan basin. As we pointed out before, this is because the ray coverage in this region is the densest. The east China part also has a pretty good resolution. Only that the resolution in the west and northwest part of Tibet region is not as good--the boundary of different velocities is more blurry, but it is still retrievable. Overall, from the resolution test, we believe our results are reliable for at least a 4 by 4 degree structure--and it is true that the structures we discussed below are all bigger than this size.

3 Results

In this session, we first present dispersion maps of Rayleigh wave group and phase velocities. The group velocity maps are updates to the earlier versions presented by Zheng et al. (Zheng et al., 2008). We then present results of 3D shear wave velocity structure inverted from the dispersion maps and discuss the major features of the 3D structure.

3.1 Dispersion maps of Rayleigh group and phase velocities

The ray coverage of our dispersion measurements is sufficient for us to invert for Rayleigh wave group and phase velocity maps at periods from 8 s to 60 s. Fig. 4 shows tomography maps for Rayleigh group and phase velocity at 10, 30, and 60 s, respectively. Because the surface velocities are sensitive to structures at different depth (with the most sensitive depth at about 1/3 of its wavelength), the tomography maps at different periods indicate the general features of 3D structure at depth. In general, our group and phase velocity maps are quite similar in major features, but they also show obvious differences in small scales, reflecting different

sensitivities of group and phase velocities to velocity changes with depth (Fig. 7).

Our tomography results show remarkable features that correlate with large-scale geological structures of China. These features confirm earlier observations from group velocity dispersions with less data (Zheng et al., 2008). Major basins in China are clearly manifested by low velocities at short periods (10 s map) including Bohai-Wan Basin (North China Basin), western part of Ordos Basin, Sichuan Basin, Qaidam Basin, Jungar Basin, and Tarim Basin (Fig. 4), which is consistent with thick sediment layers under these basins. At the same time, the stable Yangtze craton and South China Block show clear high velocities, indicating a cool and strong upper crust. When the period increases to 30 s, the dichotomy of low and high velocity in the map corresponds well with the thicker crust in the west and the thinner crust in the east. The boundary between fast and slow velocities (around longitude 108°E) shows NNE-SSW trend, coinciding with the sharp topographic change and the well-known Gravity Lineation. At 60 s, the Rayleigh velocities are influenced more by mantle lithosphere structure. The most striking feature here is a “wall” of high velocities in the north, northeast and east of the TP underneath the major basins (Tarim, Ordos, and Sichuan). We will discuss this feature further below.

3.2 Shear velocity structure

We plot the shear wave velocity maps at different depth (Fig. 5, note the regions outside the contour are not well resolved). The 3D model shows the major features that we have observed from the dispersion maps as well as new insights that are not so obvious from the dispersion maps.

Our inversion reveals significant features that correlate with surface geology. Perhaps the overall most striking feature of the shear velocity is a mosaic of very fast and very slow anomalies across the region, which provides a mirror image of the heterogeneous geology of China as we briefly summarized in the introduction.

At the shallower depth (7.5 km), low velocities are coincident with all the major basins in the region, reflecting that thick sediment layers in the basin area are well retrieved. High velocities generally appear in east China, where the stable cratons and mountains, fold belt systems are present (such as South China fold belt and Yangtze blocks). There are also obvious low velocity zones at eastern marginal seas and the south corner of the eastern Himalaya syntaxis. But when it goes to lower crust and upper mantle depth (47.5 and 75 km), the south Tibet tip becomes faster/colder.

At greater depths around 30 to 50 km, one striking feature is the slow and fast velocity dichotomy in west and east China, divided approximately by 108 degree longitude in NE direction along the east Tibet margin. The contrast is well correlated with the topography increase from east to west, as is shown in the background. This is a vivid demonstration of the thickened crust in the TP and the Tien Shan from the India-Eurasia collision: As a result, at these depths, the east part of China is already in the mantle while the TP and the Tien Shan are still in the crust.

Although most of the Tibet Plateau shows obviously low velocity, the major basins surrounding Tibet and Tienshan, including Tarim, Junggar, Sichuan and Ordos, exhibit relatively high velocity. As it goes to the

uppermost mantle (around 75 km), the higher velocity “wall” in these basins surrounding Tibet Plateau is even clearer.

Another prominent feature at mid-lower crust depth range is the low velocity regions in most of the central, eastern and southeastern part of Tibet. Fig. 6 shows cross sections of shear velocity along certain profiles. The upper row in this figure shows cross sections as plotted in figure 1. AA' is profile cross Tarim basin, Tibet Plateau and Sichuan basin, and BB' and CC' across the Tibet and the surrounding regions. The middle and bottom rows show cross sections along different latitude (from left to right, 31,34, and 39° respectively) and longitude (85, 95 and 101° from left to right). On top of each cross section, the topography is plotted. The AA' shows clearly the change of the velocities at shallow depth from basin to Tibet and to basin again, with low velocities beneath the Tarim and Sichuan basin, and the mid/lower crust low velocity regime under Tibet Plateau from about 22 to 50 km. The boundaries of Tibet Plateau coincides with the sharp change of the velocities--there's apparently high velocities surround the deep thick root of Tibet plateau.

Along these different profiles, the low velocity zones underneath Tibet Plateau are all very clear and show different depth and geometry distribution: some of them are connected to the low velocities on the surface (CC'), and some of them are shown as an isolated part in the mid/lower crust (AA'). But, no matter how the distribution and geometry changes, all the mid/lower crust low velocity zones terminate near the boundary of Tibet Plateau. By examine the velocity profiles underneath the Tibet, we found that the velocity reduction can be as much as 19%.

To demonstrate further distinct differences between different geological provinces, we compared vertical profiles of averaged velocities of a few

selected regions (Fig. 8 and 9). The major regions we selected are shown in Fig. 8. They are Tarim basin, north Tibet Plateau (NTP), Tibet Plateau (TP), the east margin of Tibet Plateau (TP Margin, including Sichuan Basin and Ordos Basin), North China blocks (NC), and Southeast China craton (SE). Since these areas represent different tectonic blocks such as basins, stable cratons, active regions that have undergone /is undergoing tectonic movements, they should show clearly different characteristics in the velocity structures (as is seen in Fig. 9).

Basically, the Tibet region (TP and NTP) has a very obvious low velocity layer at depth of ~20 to 40 km; The Tarim basin has a low velocity at shallow depth, consistent with thick sediments layer at the top, but then after 70 km, the velocity underneath Tarim basin has a higher value, indicating a strong and fast mantle lithosphere. Tibet margins (mostly Sichuan and Ordos basin) also have similar features as that of Tarim basin, but the low velocity at shallower depth and strong lithosphere root is not as fast as well. North China basin has similar velocity at shallow depth as the Tibet margin area, but it does not show strong velocity at mantle lithosphere region. Instead, the velocity structure of north china and Southeast china at deep depth are similar, since they are all old ancient cratons. But at shallow depth, Southeast China has much higher velocity---this is true because this area is a fold/mountain belt area, such the velocity reflects the high velocity.

4 Discussion

To test our 3D velocity structure in different region of China, we also compare some inter-stations dispersion measurements with the predictions from our tomography results in these blocks. The station pairs

are nearly totally located within the areas we selected, such that the comparison is more consistent.

To test our 3D velocity structure in different region of China, we also compare the observed and predicted (calculated from the averaged shear velocity structure in Fig. 9) surface wave dispersion curves for some station pairs in the selected areas (Fig. 8). The station pairs we choose are nearly all positions in certain area, such that the comparison is more consistent. It is clear that the measurements and predictions are generally consistent with each other, especially for phase velocities. The consistencies are especially well presented at stable craton or basin areas. Only that at north Tibet region and Tarim basins, the predictions sometimes may not totally reflect the value of group velocity. This reflects that our resolution in north and northwest Tibet region is not as well, as mentioned before.

In our 3D shear velocity maps, one prominent features of our shear velocity model is the mid-lower crust low velocity layers at most of the Tibet region. To test the resolve ability of our data, we do another resolution test. This time our input model is 1-D velocity model everywhere as in AK135, except in the region from latitude 27-38 degree, longitude 80-102 degree, and from depth 25-45 km and 100-140 km. In these two regions we put a low velocity layer with velocity reduction of 10%. Our purpose is to test whether the low velocity layer in the mid-lower crust can be resolved, and at the same time, we want to make sure that it can be distinguished/not contaminated from similar deeper structure.

We plotted the cross sections of input (left column) and recovered shear velocity model in Fig. 10. The recovered cross sections are along certain

latitude (30 and 35°, right two on top row) and longitude (90 and 95°, right two on bottom row). The test shows that our data and method indeed can resolve such a low velocity layer, although the amplitude of the reduction in the upper mantle region is especially underestimated. It is also need to mention here that the boundary of the low velocity layer at lower longitude side (on the top row) is not well resolved. It is not surprising because we just run out of resolution at the west Tibet margin, especially at the low latitude (see the tomography boundary in Fig. 4).

Looking at the cross sections of our shear velocity structure maps (Fig. 6), it is easily to see that the distribution of low velocity layer in most of the Tibet region is not uniform. Instead, the depth and connectivity of this layer vary at different part of the Tibet region. For example, along CC' profile, the low velocity layer connect to the surface at one end, and similar can be observed along latitude 34 degree (Fig. 6, middle panel), longitude 86 and 101 degree (Fig. 6, lower panel). At the same time, low velocity layer along AA' is more flattened as an isolated layer. however, at other locations, such as along BB', latitude 30 degree and longitude 95 degree, this layer is more like isolated blocks connected together. And the depth of the low velocity layer varies at different locations too.

Nevertheless, no matter how complicated the low velocity layer is, they all seem to terminate at the boundary of Tibet Plateau, especially confined by the high velocity basins at the margin of Tibet (as is shown in Fig. 5). The mid/lower crust low-velocity zone provides support for the channel flow model that has been proposed for the outward growth and uplift of the TP (Clark and Royden, 2000) and for the extrusion of crustal materials to the surface (Beaumont et al., 2001), but the geometry of the low velocity layer indicates that the mechanism of Tibet evolution at

different locations and time period may not be simple, and a more complex model is needed.

5 Conclusion

We collected 18 months continuous data from stations of global, regional and temporary networks from IRIS, especially from the new China National Seismic Network. Using ambient noise data of these stations, we extract the EGFs between stations pairs. Rayleigh wave group and phase velocity maps from 8~s to 60~s are then obtained. And finally, a 3D shear velocity structure in China region is inverted from these surface wave dispersion curves. Because of the CNSN and PASSCAL network stations, our data coverage are more dense and uniform. Our checker board resolution test shows that our best resolution is in central and east Tibet, Sichuan basin and east part of China, and only the structure in the northwest Tibet part is not as good.

Our results show some prominent features at different depth: 1) Near the surface, anomalously slow velocities in major basins is consistent with thick sediments underneath. 2) A slow and fast velocity contrasts in west and east part of China correlated well with the Moho depths and lithosphere thickness difference in the two regions. 3) There exists a fast (strong) mid-lower crust and mantle lithosphere in major basins surrounding the Tibet Plateau and Tianshan. These strong blocks may play an important role in confining the deformation of the Tibet Plateau to be a triangular shape. 4) In northwest TP in Qiangtang, slow anomalies extend from crust to great depth in mantle lithosphere. 5) In the central and eastern and southeastern TP, there is also big area of slow anomalies. These slow anomalies may result from partial melting.

References

- Armijo, R., Tapponnier, P., Mercier, J.L. and Han, T.L., 1986. Quaternary Extension In Southern Tibet - Field Observations And Tectonic Implications. *Journal Of Geophysical Research-Solid Earth And Planets*, 91(B14): 13803-13872.
- Barmin, M.P., Ritzwoller, M.H. and Levshin, A.L., 2001. A fast and reliable method for surface wave tomography. *Pure And Applied Geophysics*, 158(8): 1351-1375.
- Beaumont, C., Jamieson, R.A., Nguyen, M.H. and Lee, B., 2001. Himalayan tectonics explained by extrusion of a low-viscosity crustal channel coupled to focused surface denudation. *Nature*, 414(6865): 738-742.
- Bensen, G.D. et al., 2007. Processing seismic ambient noise data to obtain reliable broad-band surface wave dispersion measurements. *Geophysical Journal International*, 169(3): 1239-1260.
- Bensen, G.D., Ritzwoller, M.H. and Shapiro, N.M., 2008. Broadband ambient noise surface wave tomography across the United States. *Journal Of Geophysical Research-Solid Earth*, 113(B5).
- Blisniuk, P.M. et al., 2001. Normal faulting in central Tibet since at least 13.5 Myr ago. *Nature*, 412(6847): 628-632.
- Campillo, M. and Paul, A., 2003. Long-range correlations in the diffuse seismic coda. *Science*, 299(5606): 547-549.
- Clark, M.K. and Royden, L.H., 2000. Topographic ooze: Building the eastern margin of Tibet by lower crustal flow. *Geology*, 28(8): 703-706.
- Friederich, W., 2003. The S-velocity structure of the East Asian mantle from inversion of shear and surface waveforms. *Geophysical Journal International*, 153(1): 88-102.
- Hauck, M.L., Nelson, K.D., Brown, L.D., Zhao, W.J. and Ross, A.R., 1998. Crustal structure of the Himalayan orogen at similar to 90 degrees east longitude from Project INDEPTH deep reflection profiles. *Tectonics*, 17(4): 481-500.
- Huang, Z.X., Su, W., Peng, Y.J., Zheng, Y.J. and Li, H.Y., 2003. Rayleigh wave tomography of China and adjacent regions. *Journal Of Geophysical Research-Solid Earth*, 108(B2).
- Levshin, A.L. and Ritzwoller, M.H., 2001. Automated detection, extraction, and measurement of regional surface waves. *Pure And Applied Geophysics*, 158(8): 1531-1545.
- Li, C., van der Hilst, R.D. and Toksoz, A.N., 2006. Constraining P-wave velocity variations in the upper mantle beneath Southeast Asia. *Physics Of The Earth And Planetary Interiors*, 154(2): 180-195.

- Li, H.Y., Su, W., Wang, C.Y. and Huang, Z.X., 2009. Ambient noise Rayleigh wave tomography in western Sichuan and eastern Tibet. *Earth And Planetary Science Letters*, 282(1-4): 201-211.
- Liang, C.T. and Song, X.D., 2006. A low velocity belt beneath northern and eastern Tibetan Plateau from Pn tomography. *Geophysical Research Letters*, 33(22).
- Liang, C.T., Song, X.D. and Huang, J.L., 2004. Tomographic inversion of Pn travel times in China. *Journal Of Geophysical Research-Solid Earth*, 109(B11).
- Lin, F.C., Moschetti, M.P. and Ritzwoller, M.H., 2008. Surface wave tomography of the western United States from ambient seismic noise: Rayleigh and Love wave phase velocity maps. *Geophysical Journal International*, 173(1): 281-298.
- Molnar, P. and Tapponnier, P., 1975. Cenozoic Tectonics Of Asia - Effects Of A Continental Collision. *Science*, 189(4201): 419-426.
- Moschetti, M.P., Ritzwoller, M.H. and Shapiro, N.M., 2007. Surface wave tomography of the western United States from ambient seismic noise: Rayleigh wave group velocity maps. *Geochemistry Geophysics Geosystems*, 8.
- Nabelek, J., Chen, W.P. and Ye, H., 1987. The Tangshan Earthquake Sequence And Its Implications For The Evolution Of The North China Basin. *Journal Of Geophysical Research-Solid Earth And Planets*, 92(B12): 12615-12628.
- Nelson, K.D. et al., 1996. Partially molten middle crust beneath southern Tibet: Synthesis of project INDEPTH results. *Science*, 274(5293): 1684-1688.
- Paul, A., Campillo, M., Margerin, L., Larose, E. and Derode, A., 2005. Empirical synthesis of time-asymmetrical Green functions from the correlation of coda waves. *Journal Of Geophysical Research-Solid Earth*, 110(B8).
- Ritzwoller, M.H., Levshin, A.L., Ratnikova, L.I. and Egorkin, A.A., 1998. Intermediate-period group-velocity maps across Central Asia, western China and parts of the Middle East. *Geophysical Journal International*, 134(2): 315-328.
- Sabra, K.G., Gerstoft, P., Roux, P., Kuperman, W.A. and Fehler, M.C., 2005a. Extracting time-domain Green's function estimates from ambient seismic noise. *Geophysical Research Letters*, 32(3).
- Sabra, K.G., Gerstoft, P., Roux, P., Kuperman, W.A. and Fehler, M.C., 2005b. Surface wave tomography from microseisms in Southern California. *Geophysical Research Letters*, 32(14).
- Sabra, K.G., Roux, P. and Kuperman, W.A., 2005c. Emergence rate of the time-domain Green's function from the ambient noise cross-

- correlation function. *Journal Of The Acoustical Society Of America*, 118(6): 3524-3531.
- Sandvol, E., Ni, J., Kind, R. and Zhao, W.J., 1997. Seismic anisotropy beneath the southern Himalayas-Tibet collision zone. *Journal Of Geophysical Research-Solid Earth*, 102(B8): 17813-17823.
- Shapiro, N.M. and Campillo, M., 2004. Emergence of broadband Rayleigh waves from correlations of the ambient seismic noise. *Geophysical Research Letters*, 31(7).
- Shapiro, N.M., Campillo, M., Stehly, L. and Ritzwoller, M.H., 2005. High-resolution surface-wave tomography from ambient seismic noise. *Science*, 307(5715): 1615-1618.
- Shapiro, N.M., Ritzwoller, M.H., Molnar, P. and Levin, V., 2004. Thinning and flow of Tibetan crust constrained by seismic anisotropy. *Science*, 305(5681): 233-236.
- Sun, Y.S. and Toksoz, M.N., 2006. Crustal structure of China and surrounding regions from P wave travelttime tomography. *Journal Of Geophysical Research-Solid Earth*, 111(B3).
- Tilmann, F. and Ni, J., 2003. Seismic imaging of the downwelling Indian lithosphere beneath central Tibet. *Science*, 300(5624): 1424-1427.
- Tseng, T.L., Chen, W.P. and Nowack, R.L., 2009. Northward thinning of Tibetan crust revealed by virtual seismic profiles. *Geophysical Research Letters*, 36.
- Turner, S. et al., 1996. Post-collision, shoshonitic volcanism on the Tibetan plateau: Implications for convective thinning of the lithosphere and the source of ocean island basalts. *Journal Of Petrology*, 37(1): 45-71.
- Williams, H., Turner, S., Kelley, S. and Harris, N., 2001. Age and composition of dikes in Southern Tibet: New constraints on the timing of east-west extension and its relationship to postcollisional volcanism. *Geology*, 29(4): 339-342.
- Wu, F.T., Levshin, A.L. and Kozhevnikov, V.M., 1997. Rayleigh wave group velocity tomography of Siberia, China and the vicinity. *Pure And Applied Geophysics*, 149(3): 447-473.
- Yang, Y.J., Ritzwoller, M.H., Levshin, A.L. and Shapiro, N.M., 2007. Ambient noise rayleigh wave tomography across Europe. *Geophysical Journal International*, 168(1): 259-274.
- Yao, H.J., Beghein, C. and van der Hilst, R.D., 2008. Surface wave array tomography in SE Tibet from ambient seismic noise and two-station analysis - II. Crustal and upper-mantle structure. *Geophysical Journal International*, 173(1): 205-219.
- Yin, A. and Harrison, T.M., 2000. Geologic evolution of the Himalayan-Tibetan orogen. *Annual Review Of Earth And Planetary Sciences*, 28: 211-280.

- Ying, J.F., Zhang, H.F., Kita, N., Morishita, Y. and Shimoda, G., 2006. Nature and evolution of late cretaceous lithospheric mantle beneath the eastern North China Craton: Constraints from petrology and geochemistry of peridotitic xenoliths from Junan, Shandong Province, China. *Earth And Planetary Science Letters*, 244(3-4): 622-638.
- Zhang, P.Z. et al., 2004. Continuous deformation of the Tibetan Plateau from global positioning system data. *Geology*, 32(9): 809-812.
- Zhao, W. et al., 2001. Crustal structure of central Tibet as derived from project INDEPTH wide-angle seismic data. *Geophysical Journal International*, 145(2): 486-498.
- Zheng, S.H., Sun, X.L., Song, X.D., Yang, Y.J. and Ritzwoller, M.H., 2008. Surface wave tomography of China from ambient seismic noise correlation. *Geochemistry Geophysics Geosystems*, 9.

Figs

Fig 1: (a) Maps of China and surrounding areas in this study. Gray lines mark the major tectonic boundaries (thick lines) and major basins (thin lines). The basins include Tarim (TRM), Junggar (JG), Qaidam (QD), Sichuan (SC), Ordos (OD), Bohai Wan (BHW) and Songliao (SL) basin. The blocks include Songpan-Ganzi, Qiangtan, Lhasa and Himalaya block in Tibet region and Sino-Korea Craton, Yangtze block and South China fold belt in East China. Plotted on the background is the topography in this region. (b) Distribution of seismic stations used in this study, including CNSN stations (solid white triangles), global and regional stations in the surrounding areas (solid pink triangles) and temporary PASSCAL stations (open blue triangles). AA', BB' and CC' are cross section profiles shown in Fig. 6.

Fig 2: (Top) Dispersion measurement numbers at different periods for Rayleigh group (solid) and phase (dashed) velocities. (bottom) Ray path density at 20s period. The ray density is the number of rays in 1 by 1 degree cells. The coverage for shorter and longer periods deteriorates, but the spatial pattern remains similar.

Fig. 3: Checker board resolution tests of our surface wave inversion. The input model (upper left corner) is a 4 by 4 degree checkers with 5% velocity perturbation with respect to AK135 model. Retrieved models at different depths (labeled on lower left corner) are also shown.

Fig. 4: Rayleigh wave group (left column) and phase (right column) velocity maps at periods of 10, 30, and 60 s, respectively. Plotted on the background are topography and the major tectonic boundaries and basins as in Fig. 1. The dashed line is 800 km resolution contour for 20 s tomography map. Note that the 10 s maps delineate the major basins with slow velocities clearly; the 30 s maps shows two different regimes in the east and west, corresponding to the crust thickness difference in the east and west. In general, the group and phase velocity maps are similar, especially at short periods.

Fig 5: Shear wave velocity at 7.5 km, 22.5 km, 32.5 km, 47.5 km, 75 km and 95 km. Dashed line is the same as in Fig. 4. Results show some remarkable features for continental China and in particular Tibet Plateau, including slow sedimentary of all the major basins at shallower depth (7.5 km), striking wide spread mid/lower crust low velocities in most of the Tibet region (32.5 km, 47.5 km), fast mid-lower crust and mantle

lithosphere in major basins surrounding the Tibet Plateau (Tarim, Ordos, and Sichuan) (75 km).

Fig 6: Vertical cross sections of shear velocity maps. White lines represent the crust thickness from Crust2.0 model (<http://igppweb.ucsd.edu/~gabi/rem.html>). Locations of AA', BB' and CC' in first row are shown in Fig. 1. The center and bottom rows are along different latitude (from left to right, 30, 31 and 34° latitude) and longitude (from left to right, 85, 95, and 101° longitude), respectively. These cross section maps show clearly the mid-lower crust low velocity layers at different regions in Tibet Plateau, and these low velocity layers are diverse in geometry, depth distribution, and even the intensity of the velocity reduction, suggesting the mechanism of Tibet media flow is complicated.

Fig. 7: Sensitivity kernels of fundamental Rayleigh group and phase velocities at 10~s, 30~s and 60~s.

Fig 8: (Top) Maps of major blocks (white polygons) with station pairs mostly positioned in these blocks (black triangles). These blocks include Tarim, north Tibet Plateau (NTP), Tibet Plateau (TP), east Tibet Plateau margin (TP Margin), North China basin (NC) and Southeast China (SE). (Bottom) Comparisons of Rayleigh wave group, phase velocity measurements (dashed lines) and predictions (solid lines) from averaged block models as shown in Fig. 9. The observed and predicted velocities generally agree very well in all the selected blocks, suggesting our inversion results represent the data characteristics.

Fig 9: Averaged shear velocity models in major blocks in Fig. 8. The averaged velocity model shows clearly different characteristics of the crust and upper mantle underneath.

Fig 10: Resolution test of low velocity region. The input is a uniform model with two low velocity layers underneath Tibet region (latitude 27 to 38°, longitude 80 to 102°). One layer is in the mid-lower crust (25 to 45 km depth) and one in upper mantle region (100 to 140 km depth), with velocity reduction of 10%. The top row are cross sections of input (left) and retrieved models (right two) along latitude, and the bottom row are input (left) and retrieved models (right two) along longitude. The horizontal axis in top and bottom row is longitude and latitude, respectively. The recovered cross sections shown here are along latitude 30 and 35°, longitude 90 and 95°, respectively.

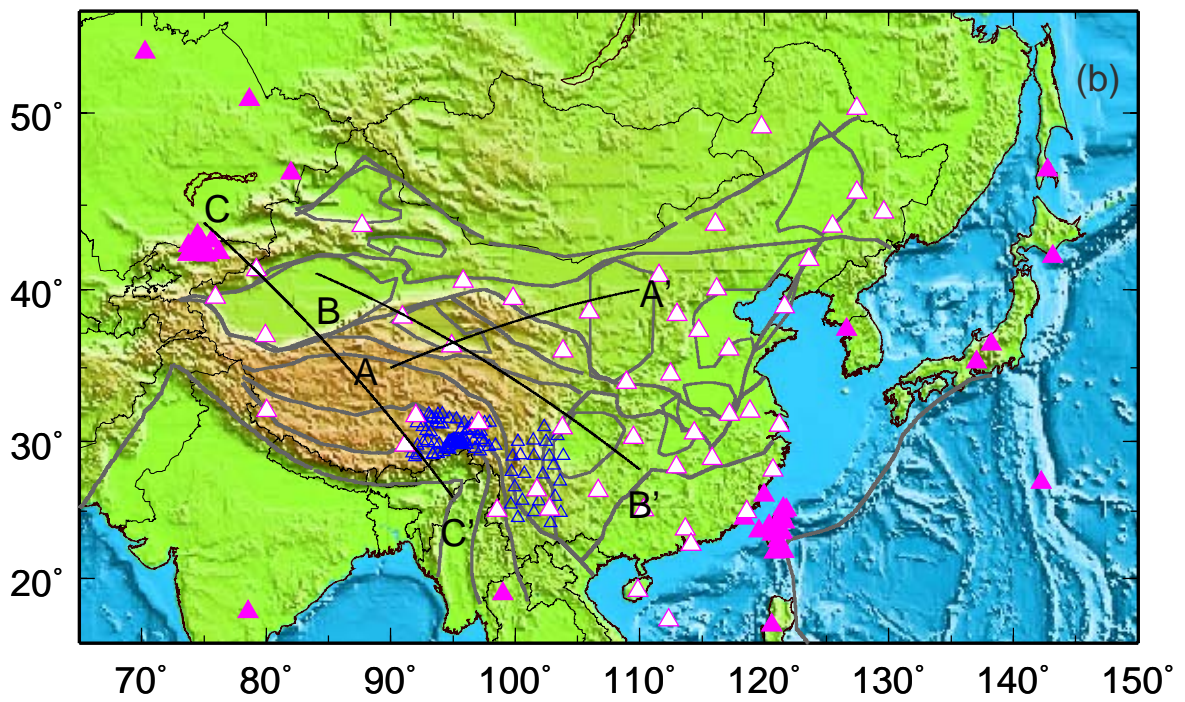
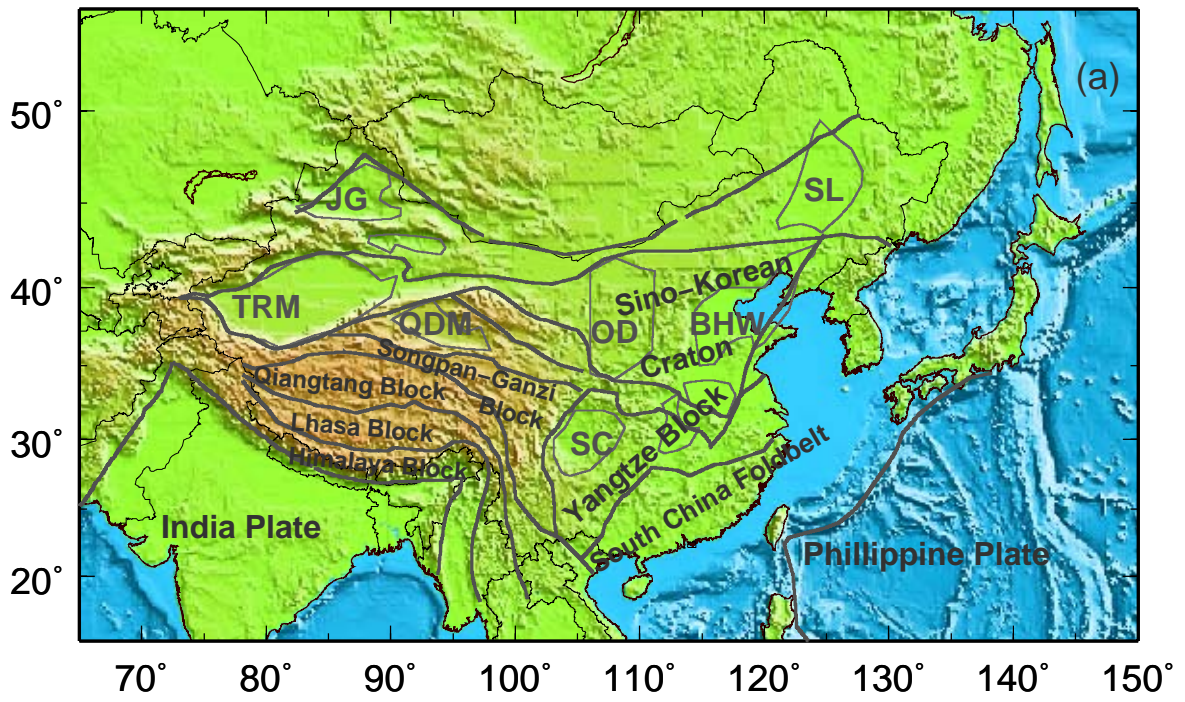


Fig. 1

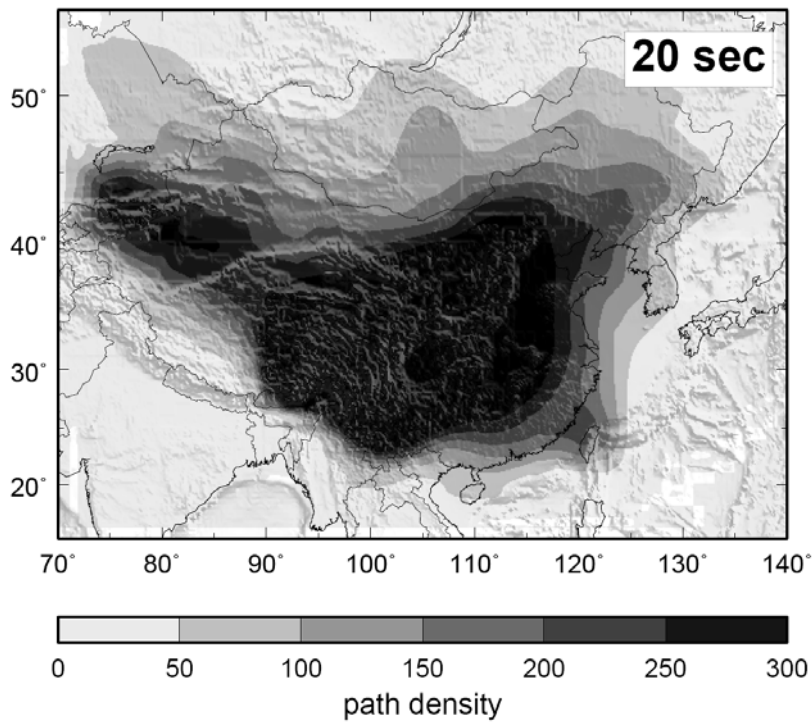
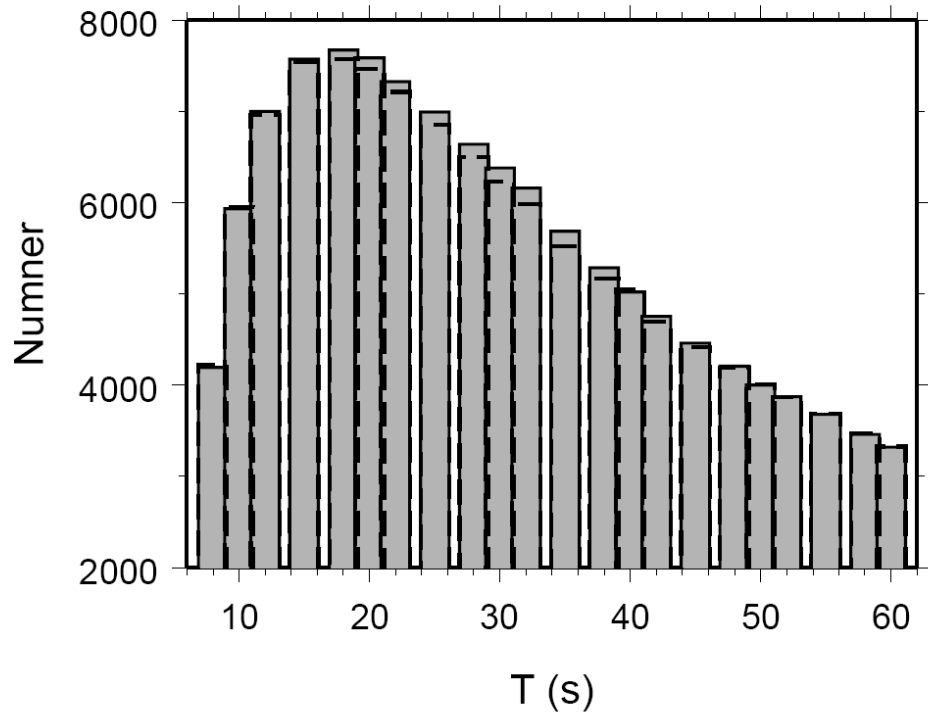


Fig. 2

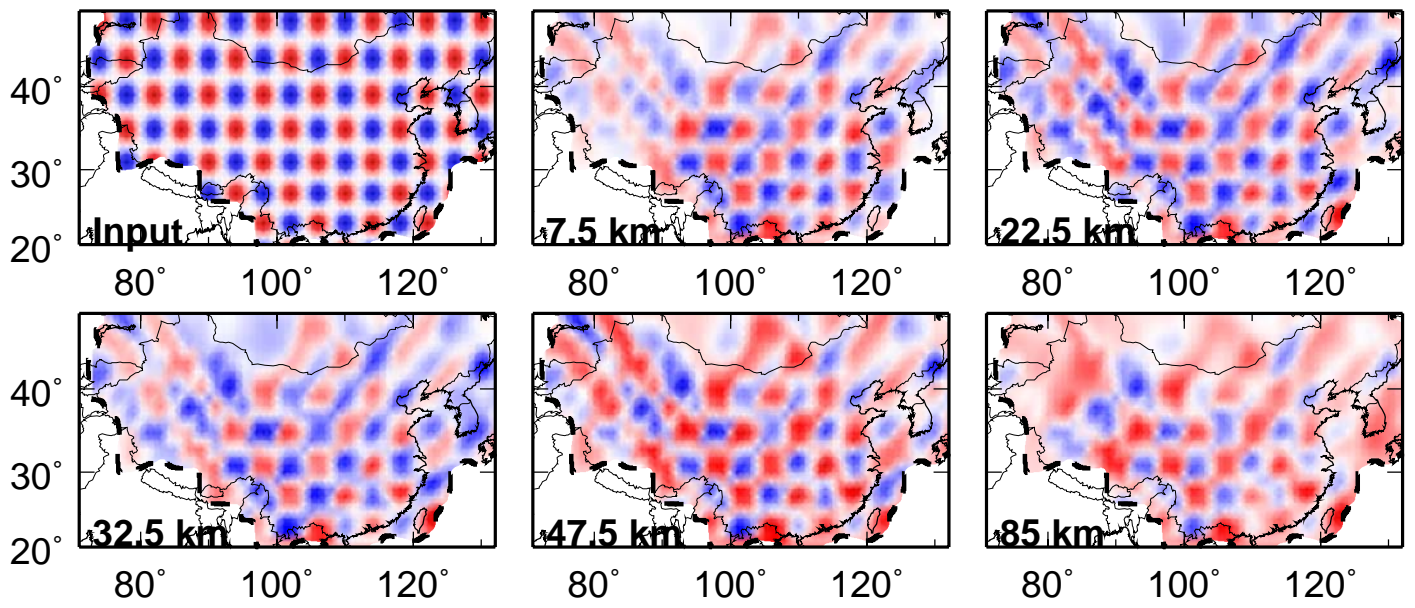


Fig. 3

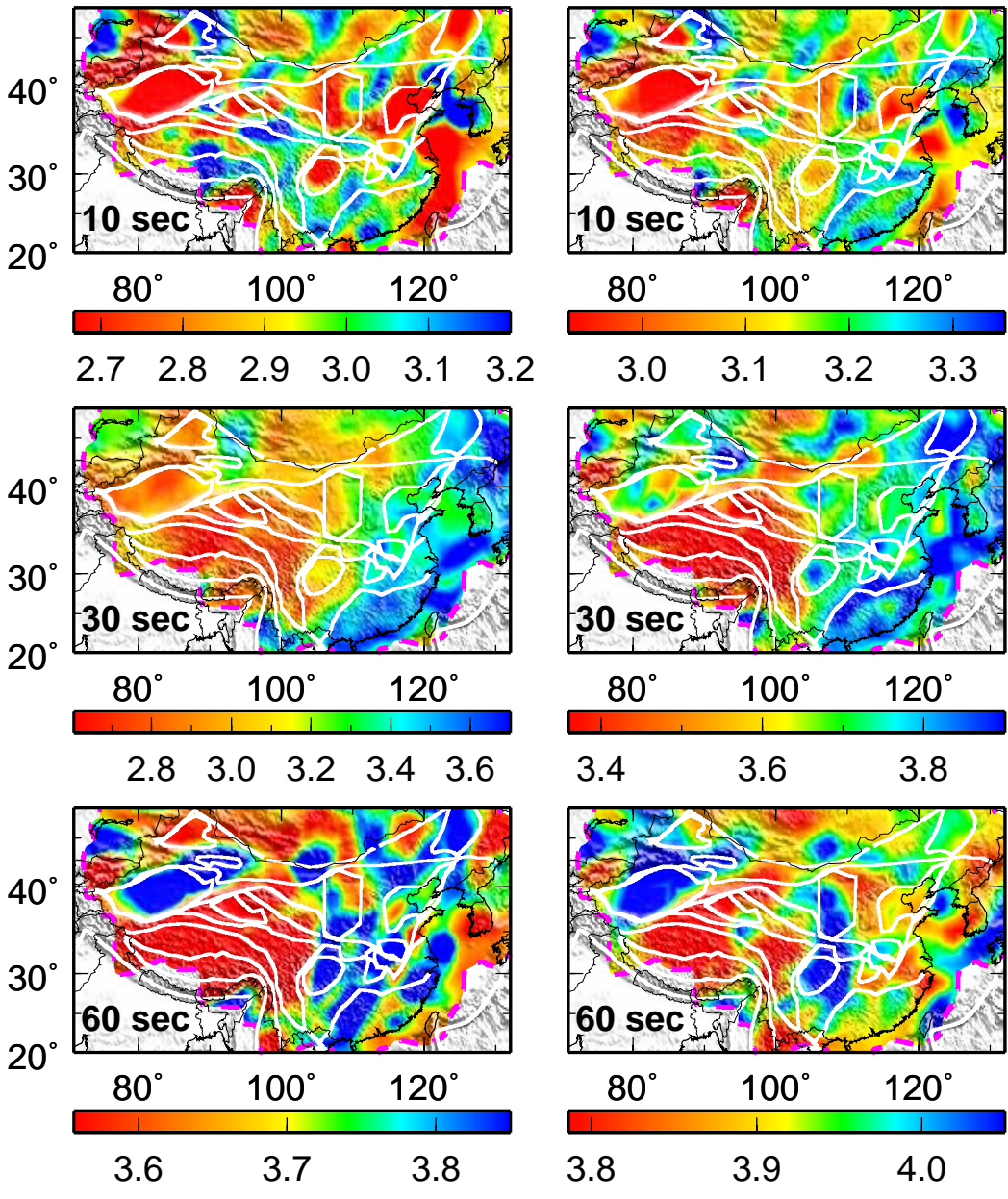


Fig. 4

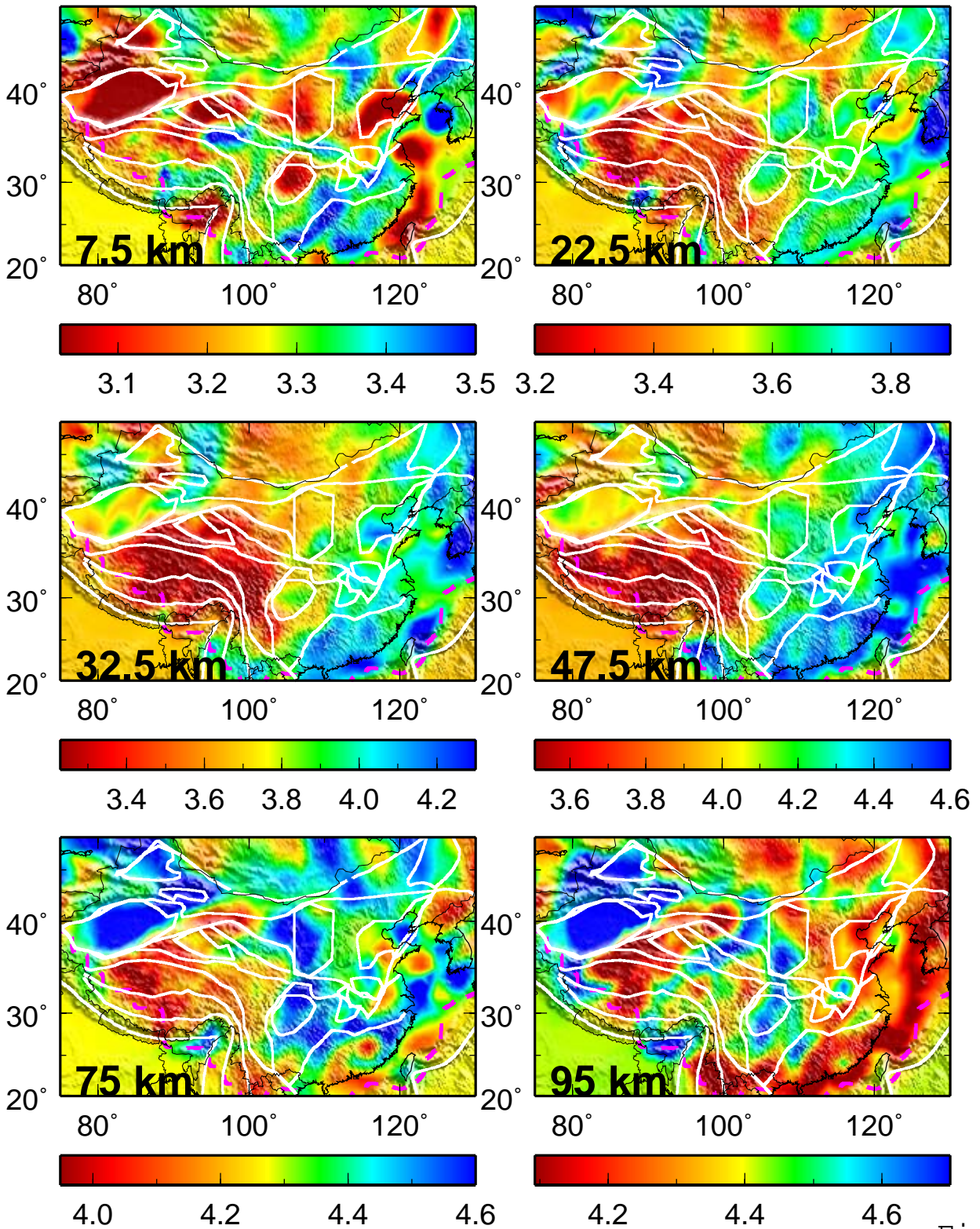


Fig. 5

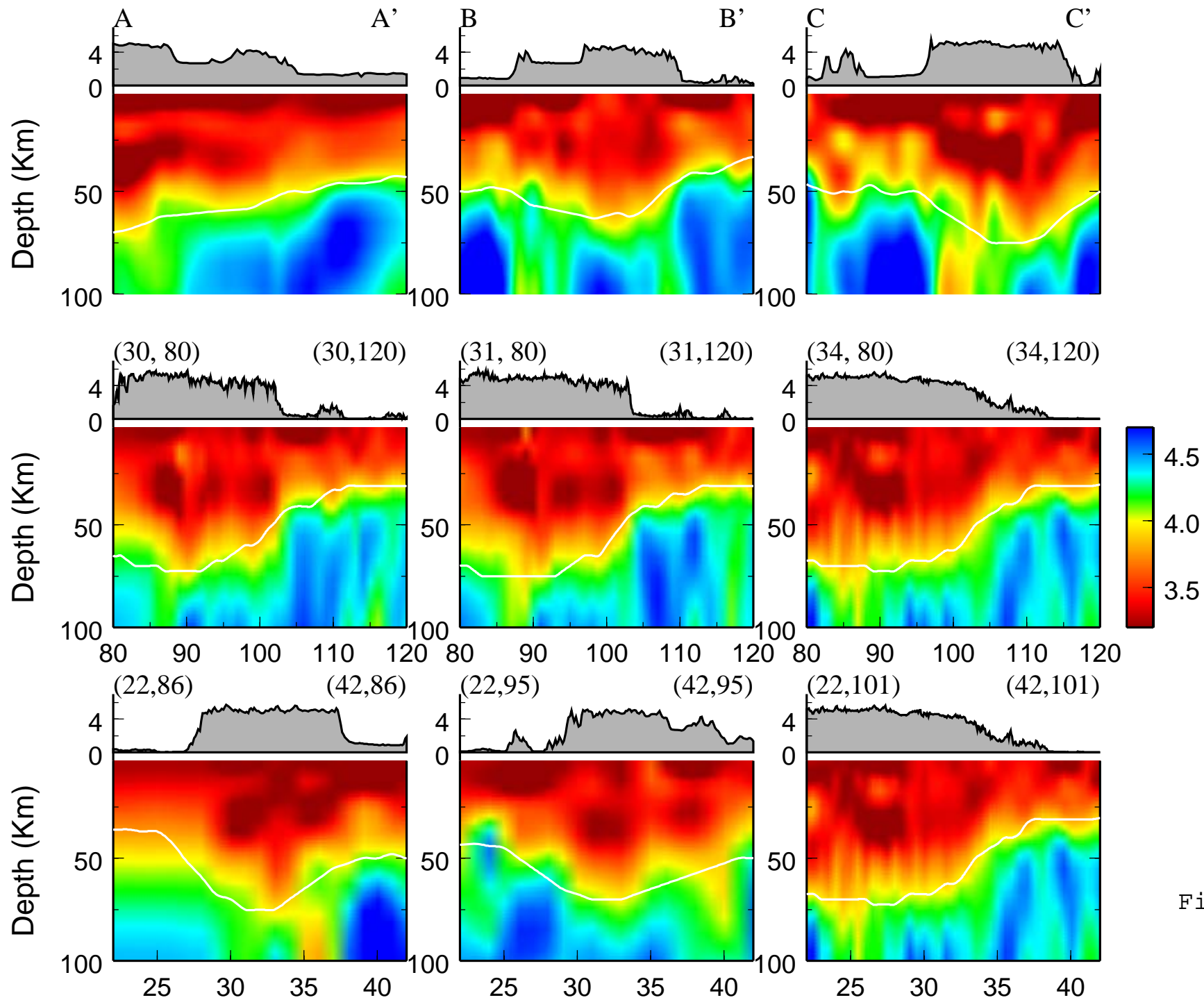


Fig. 6

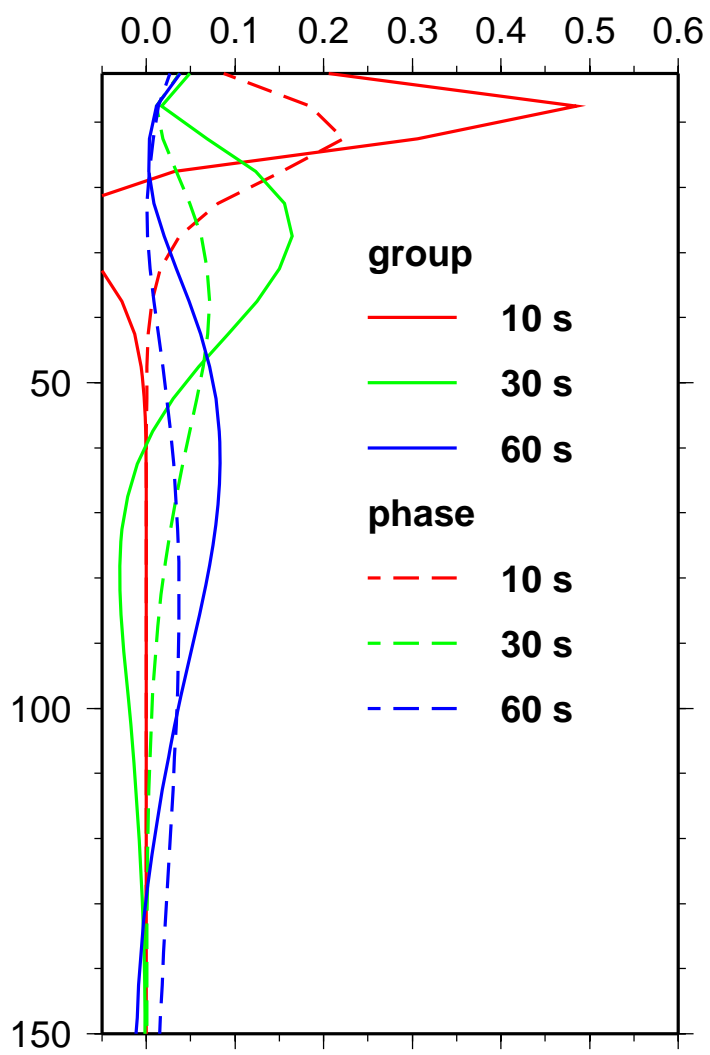


Fig. 7

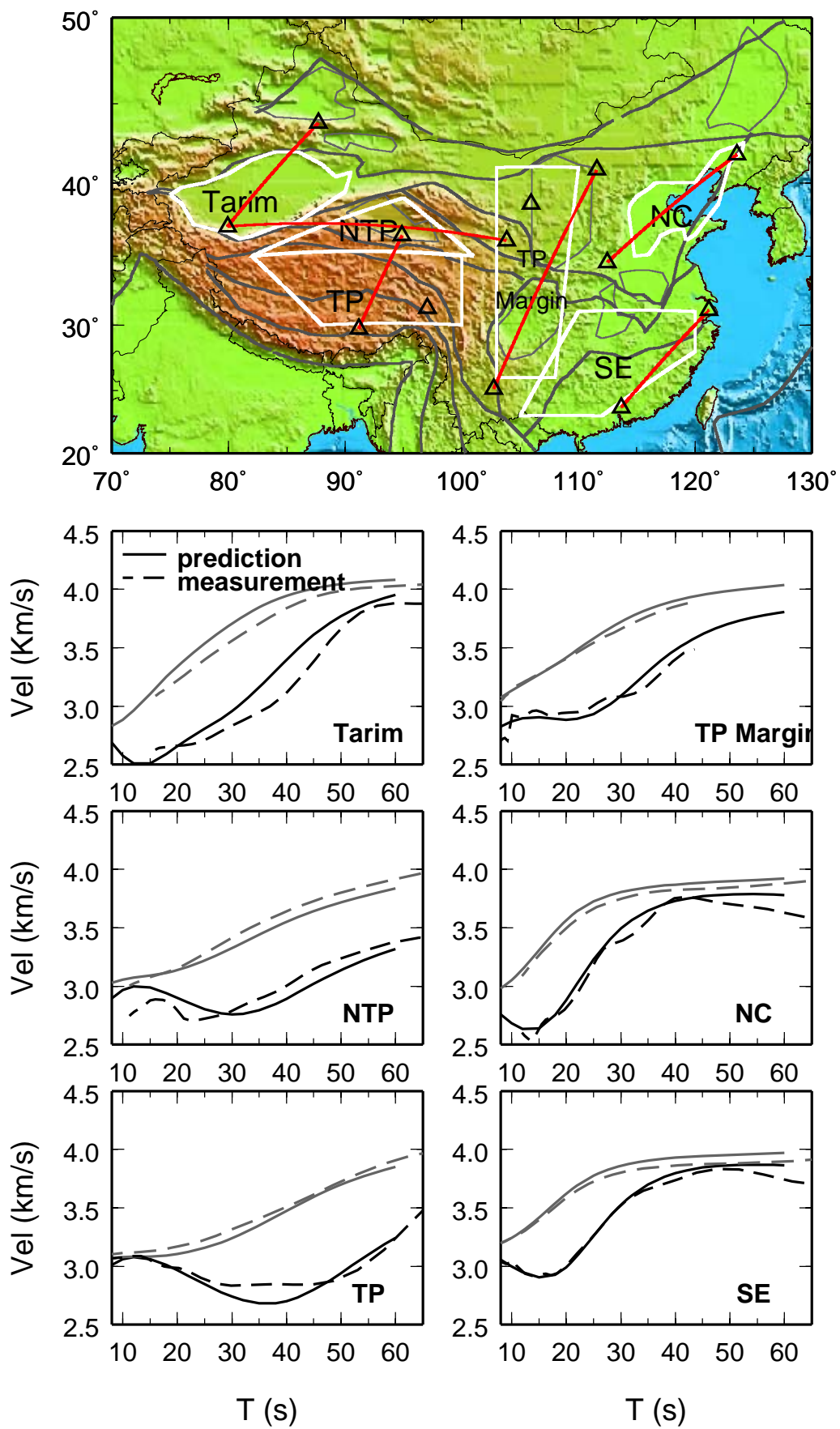


Fig. 8

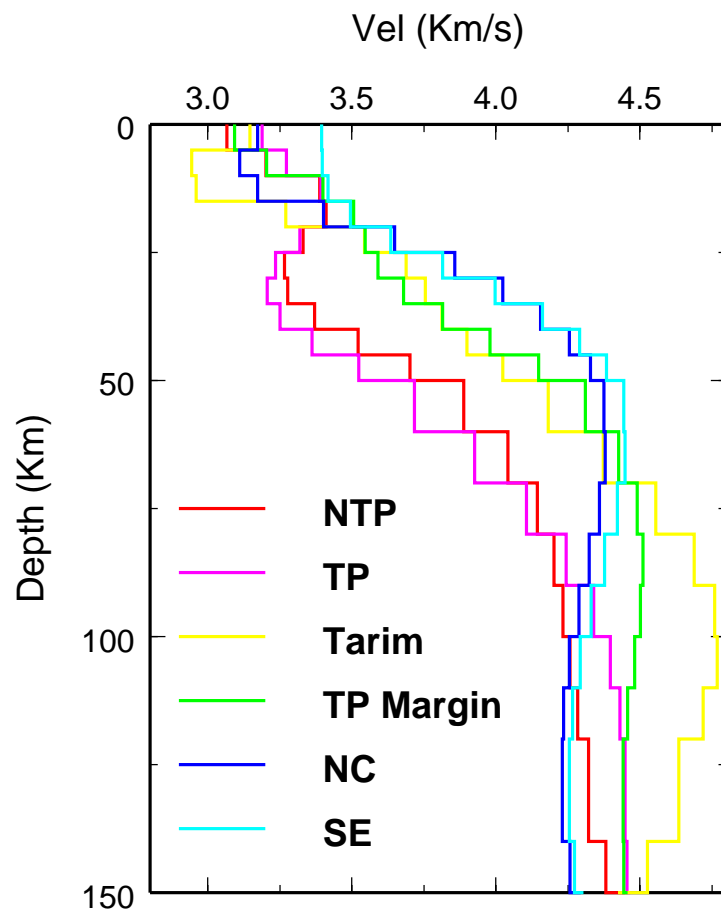


Fig. 9

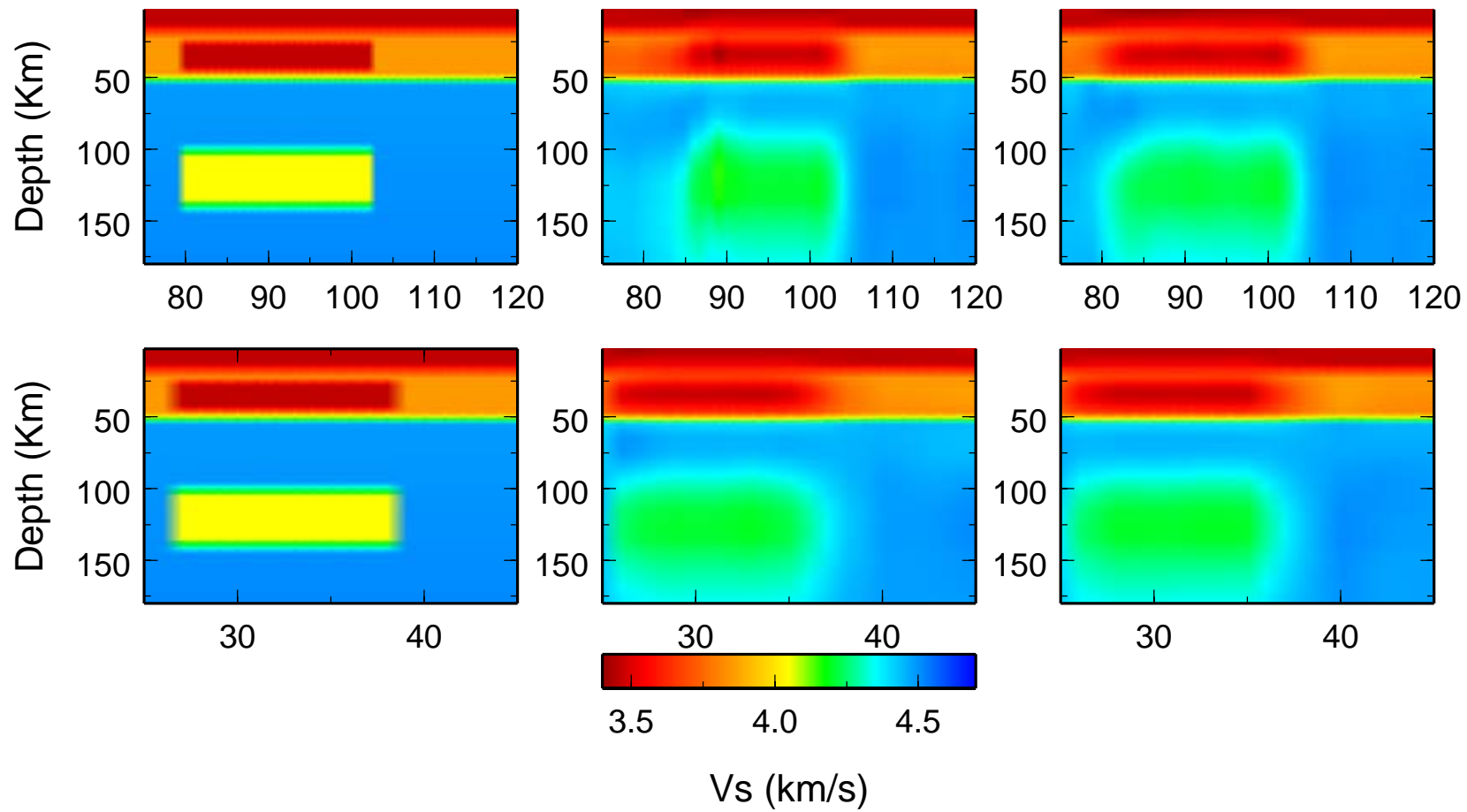


Fig. 10